Photonic Network Communications (2025) 50:1
https://doi.org/10.1007/s11107-025-01031-0

ORIGINAL PAPER

Performance analysis of a UAV-integrated RIS-aided MRR-FSO system utilizing wavelength and time diversity techniques

Amr G. AbdElKader[1] · Ahmed Allam[2] · Kazutoshi Kato[3] · Hossam M. H. Shalaby[4]

Received: 20 April 2024 / Accepted: 5 June 2025

Abstract

This paper proposes an unmanned aerial vehicles (UAV)-integrated reconfigurable intelligent surface (RIS)-assisted modulating retroreflector (MRR) free-space optical (FSO) communication system, enhanced with wavelength diversity (WD) and time diversity (TD) techniques, to address the challenges posed by dynamic channel conditions such as fog, gamma–gamma turbulence, and pointing errors. The integration of UAVs, programmable RISs, and passive MRRs forms a scalable and modular architecture—referred to as the UAV-integrated RIS-assisted MRR-FSO system—that significantly enhances system availability, adaptability, and energy efficiency. Analytical expressions for key performance metrics, including outage probability, average bit error rate (BER), and maximum effective bit rate, are derived and validated through Monte Carlo (MC) simulations, demonstrating a high degree of agreement with the theoretical results. Numerical evaluations show that the proposed system achieves up to 75% BER reduction and a 60% improvement in outage probability compared to conventional UAV-FSO systems. Furthermore, the incorporation of RIS and MRR components leads to up to 40% enhancement in energy efficiency, along with substantial reductions in hardware complexity and deployment cost. The WD design offers up to 2× higher effective data rate and a 2–5× improvement in spectral efficiency, positioning the system as a strong candidate for reliable, energy-efficient, and adaptive UAV-based optical backhaul solutions in future 6 G networks.

1 Introduction

In 5 G networks, establishing high-data-rate links between dense traffic zones and the core network remains challenging. While fiber optics offer reliability, their deployment is often costly or impractical. FSO systems provide an appealing alternative due to their large bandwidth, rapid deployment, license-free operation, and immunity to electromagnetic interference [1].

The impracticality of deploying FSO systems in various applications, attributed to the lack of a direct link and the presence of barriers causing dead zones in wireless communication, prompts the exploration of RIS as a promising solution [2]. Utilizing planar meta-surfaces with integrated electronics, RISs offer precise control over the phase, amplitude, and polarization of incoming signals. RIS emerges as an effective alternative to active relay techniques, enhancing FSO system performance without intricate processing at the relay point [3]. Recent studies extensively analyze RIS-enabled wireless systems across diverse communication mediums, including radio frequency (RF) transmissions [4], FSO systems [5], and hybrid RF-FSO setups [6]. Furthermore, recent proposals explore the application of RIS in connected autonomous vehicles and vehicular networks, considering the advantages it brings to traditional wireless communications [7].

In traditional FSO setups, two identical transceivers serve as connecting terminals, utilizing a narrow laser beam in an

✉ Amr G. AbdElKader
amr.abdelkader@ejust.edu.eg

Ahmed Allam
ahmed.allam@ejust.edu.eg

Kazutoshi Kato
kato@ed.kyushu-u.ac.jp

Hossam M. H. Shalaby
hossam.shalaby@utoledo.edu

1 Faculty of Engineering, Alexandria University, Alexandria 21544, Egypt

2 Department of Electronics and Communications Engineering, Egypt-Japan University of Science and Technology (E-JUST), Alexandria 21934, Egypt

3 Graduate School of Information Science and Electrical Engineering, Kyushu University, Fukuoka 819-0395, Japan

4 Department of Electrical Engineering and Computer Science, University of Toledo, Toledo, USA

Published online: 02 July 2025

unguided atmospheric environment for data transmission. This design, while offering advantages like reduced power consumption and improved anti-interception capabilities, requires sophisticated Pointing, Acquisition, and Tracking (PAT) systems in both transceivers, leading to challenges in power consumption and increased dimensions [2]. An interesting alternative involves configuring an asymmetrical FSO system by replacing one transceiver with an MRR terminal, comprising an MRR device and a photodetector. MRRs are constructed using light modulators and passive retroreflectors, with various fabrication techniques, including multiple quantum wells, micro-electromechanical systems, ferroelectric piezoelectric lead zirconate titanate thin films, and liquid crystals for modulators. Commonly used retroreflectors include the corner cube and cat's eye reflectors [8]. Research focuses on advancing MRR devices [8] and practically implementing MRR-FSO networks [9], highlighting the viability of MRR-FSO technology due to its low-power modulators and compact retroreflectors, suitable for diverse applications such as communication with UAVs.

To combat the composite fading effect on FSO links, various methods commonly used in wireless radio have been explored. These methods encompass spatial, wavelength, and time diversity to overcome fading effects and enhance system performance. Spatial diversity involves integrating multiple transceivers in an FSO system at different positions, transmitting and receiving replicas to reduce the BER [10]. WD employs a composite transmitter (CT), simultaneously transmitting signals at various wavelengths to multiple receivers, mitigating atmospheric effects, and enhancing reliability [11]. TD, outlined in [12], utilizes a single transceiver, transmitting the signal repeatedly during distinct time slots to enhance reliability in communication systems. While WD offers advantages, it requires complex equipment and faces alignment challenges, and TD, though simpler to implement, has drawbacks like reduced data rate and increased latency [12].

In this work, our investigation focuses on leveraging the benefits provided by the RIS module, the MRR terminal, and the UAV in a UAV-integrated RIS-aided MRR-FSO system that utilizes WD and TD techniques.

As far as our current knowledge extends, there has been no previous exploration of WD and TD techniques in a UAV-integrated RIS-aided MRR-FSO system utilizing intensity modulation/direct detection (IM/DD) and operating in a channel environment affected by fog, gamma–gamma (G–G) turbulence, and pointing errors (PEs). This unique focus is the central theme of this manuscript.

The primary contributions presented in this paper include the derivation of the PDF describing the combined statistical effects of fog with G-G turbulence and PEs in a UAV-integrated RIS-aided MRR-FSO system, expressed using the multivariate Fox H function (MFHF). This is accomplished by considering the summation of products involving independent non-identically distributed (i.ni.d) fading coefficients. Additionally, we apply this derived result to formulate closed-form analytical expressions for the PDF and CDF of the instantaneous electrical SNR (γ) for the aforementioned system. The established PDF and CDF of γ are then utilized to assess the system's performance through the derivation of expressions for P_{out}, $\overline{P}_b$, and R_{eff} (for the TD scheme only), incorporating both WD and TD techniques, all expressed in terms of the MFHF. Finally, we provide numerical results for typical scenarios and varying atmospheric turbulence and PE conditions.

In the landscape of 5 G and emerging 6 G technologies, the proposed system exhibits a high degree of adaptability across multiple application domains. For ultra-reliable low-latency communication scenarios—such as UAV-assisted backhaul and emergency response operations—the architecture provides strong resilience against optical turbulence and alignment errors [13]. In the context of enhanced mobile broadband, the WD configuration facilitates parallel multi-wavelength transmission, thereby improving both the effective data rate and spectral efficiency [14]. Additionally, the incorporation of passive elements such as MRRs and RISs significantly boosts energy efficiency and enables modular scalability. These characteristics render the proposed framework highly suitable for massive machine-type communication applications [15]. Collectively, these attributes underscore the system's potential as a versatile and energy-conscious solution for next-generation optical wireless backhaul in 5 G and beyond.

The structure of this paper is as follows: Sect. 2 presents an overview of the system and channel models. Section 3 conducts a statistical analysis of the UAV-integrated RIS-aided MRR-FSO system. Performance analysis, including closed-form expressions for P_{out}, $\overline{P}_b$, and R_{eff} (only for the TD scheme), is discussed in Sect. 4. Section 5 delves into the numerical results and their discussion. Lastly, Sect. 6 summarizes the conclusions drawn from this study.

2 System and channel models

Consider a scenario where a two-way optical wireless communication system is established using a RIS mounted on a UAV and a MRR, as illustrated in Fig. 1. This system enables bidirectional data exchange between a transmitter/receiver and a remote MRR-equipped user terminal by exploiting dynamic optical beam steering and retro-modulation.

Fig. 1 System model

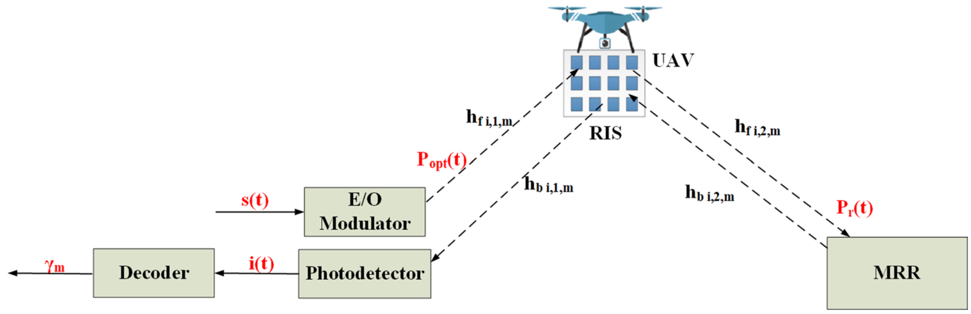

The process begins with the generation of an electrical input data signal $s(t) \in \{-1, +1\}$, representing a binary bitstream typically used in On-Off Keying (OOK) modulation. This signal is passed to an Electro-Optical (E/O) Modulator, which converts the electrical binary data into an intensity-modulated optical signal. The resulting optical signal is expressed as:

$$P_{\text{opt}}(t) = P_0[1 + \eta \cdot s(t)] \tag{1}$$

where P_0 is the average optical power and η is the modulation index that establishes the modulation depth. The optical signal $P_{\text{opt}}(t)$ is transmitted to a RIS array attached to a UAV. Acting as a passive, adjustable beam-steering device, the RIS modifies the phase shifts of incoming light waves to guide the beam. In this configuration, the RIS directs the optical beam toward the user terminal with MRR, utilizing the forward channel coefficients $h_{f_{i,1,m}}$ and $h_{f_{i,2,m}}$.

When the optical signal reaches the MRR, it is received and undergoes retro-modulation. The MRR, often based on MEMS or liquid crystal modulators, adds a new modulation to the reflected signal without requiring any internal power. This modulated signal is then reflected back along the same trajectory. The RIS on the UAV captures the retroreflected signal and reorients it toward the receiver using the backward channel coefficients $h_{b_{i,2,m}}$ and $h_{b_{i,1,m}}$. A photodetector at the receiver converts the modulated optical signal into an electrical current, expressed as:

$$i(t) = R \cdot P_r(t) \tag{2}$$

where R represents the photodiode's responsivity. This electrical signal $i(t)$ is then processed by a decoder for signal recovery and passed to a module for estimating the SNR and BER. The SNR is determined by the following equation:

$$\gamma = \frac{(R \cdot P_r)^2}{\sigma^2} \tag{3}$$

where σ^2 denotes the noise variance. The BER is then estimated using the Q-function as:

$$\bar{P}_b = Q(2\gamma) \tag{4}$$

This proposed system is particularly well suited for dynamic or obstructed environments, offering a power-efficient and flexible solution for enhancing communication range and quality without requiring onboard power at the user terminal.

The integration of WD into the UAV-integrated RIS-aided MRR-FSO system involves a model with M distinct transceivers. Simultaneously, these transmitters send M replicas of the signal at M different operational wavelengths. Each signal replica, denoted as the m^{th} signal for $m = 1, \ldots, M$, is exclusively received by the corresponding m^{th} receiver, configured to identify only the m^{th} wavelength. Optical receivers operate optimally within a narrow region around their operational wavelength, ensuring that the m^{th} signal in the m^{th} receiver originates solely from the m^{th} transmitter transmitting at the designated m^{th} wavelength.

This specificity in wavelength transmission and reception forms the basis of the WD scheme, where a CT transmits along M wavelength branches to align with the M receivers, as outlined in [16]. Additionally, when examining link distances of a few kilometers, these M receivers exhibit practical independence, especially when the photodetectors' aperture separation is measured in centimeters [17].

Using a similar method, the incorporation of a TD scheme in the considered system can be represented as a communication system employing a single transmitter that sends M replicas of the signal across M distinct time slots. On the receiving end, a receiver system utilizes the optimal combining (OC) reception technique for these M signal copies. This procedure is similar to the combined operation of a single transmitter transmitting through M channels, where M receivers are positioned at the receiving end, as the situation associated with WD.

To facilitate the physical implementation of the proposed system, a three-dimensional spatial layout is considered. The positions of the CT, the UAV-mounted RIS, and the MRR unit are represented by the vectors

$\mathbf{r}_{\mathrm{CT}} = (x_{\mathrm{CT}}, y_{\mathrm{CT}}, h_{\mathrm{CT}})$, $\mathbf{r}_{\mathrm{RIS}} = (x_{\mathrm{RIS}}, y_{\mathrm{RIS}}, h_{\mathrm{RIS}})$, $\mathbf{r}_{\mathrm{MRR}} = (x_{\mathrm{MRR}}, y_{\mathrm{MRR}}, h_{\mathrm{MRR}})$, respectively. The spatial relationship between two nodes, $i \to j$, is defined using azimuth and elevation angles, which are computed as follows [18]:

$$\phi_{ij} = \tan^{-1}\left(\frac{y_j - y_i}{x_j - x_i}\right), \quad \theta_{ij} = \sin^{-1}\left(\frac{h_j - h_i}{\|\mathbf{r}_j - \mathbf{r}_i\|}\right), \tag{5}$$

where $\|\mathbf{r}_j - \mathbf{r}_i\|$ represents the Euclidean distance between the nodes. These angular measurements are essential for determining the feasibility of the LoS path and for effectively guiding the RIS beam.

The field of view (FoV) of the photodetector, denoted by θ_{FoV}, determines the maximum angular deviation allowed for proper detection. Communication is successful only if the following condition holds:

$$|\theta_{\mathrm{incident}} - \theta_{\mathrm{receiver}}| \leq \theta_{\mathrm{FoV}}. \tag{6}$$

The optical signal produced by the transceiver follows a Gaussian beam pattern, which is characterized by a divergence angle θ_d. The received optical power at a distance L is represented by:

$$P_r = P_t \cdot \eta \cdot \exp\left(-2\left(\frac{r}{w(L)}\right)^2\right), \tag{7}$$

where P_t is the transmitted power, η encompasses system and atmospheric losses, r is the radial displacement at the receiver plane, and $w(L)$ is the beam radius at distance L, given by:

$$w(L) = w_0\sqrt{1 + \left(\frac{\lambda L}{\pi w_0^2}\right)^2}, \tag{8}$$

with w_0 representing the beam waist at the focal point and λ the operating wavelength. These expressions are fundamental for analyzing power attenuation due to misalignment and beam spread, particularly in systems relying on RIS-assisted optical reflection.

The UAV's altitude h_{RIS} and horizontal coordinates $(x_{\mathrm{RIS}}, y_{\mathrm{RIS}})$ are adaptively determined to ensure that the indirect optical path from the CT to the MRR via the RIS satisfies both angular alignment and range constraints, while remaining within the UAV's operational envelope. These spatial and directional constraints are integrated into the Monte Carlo (MC) simulations presented in Sect. 5, providing evidence of the system's practical viability and experimental reproducibility with currently available hardware.

To assess the spatial coverage of the proposed RIS-aided MRR-FSO system, we derive expressions for its 2D and 3D coverage boundaries based on geometric constraints such as beam divergence, photodetector FoV, UAV altitude, and azimuth/elevation angles. These expressions define the area or volume in which the received SNR exceeds a threshold γ_{th}. The resulting beam footprint diameter at the receiver plane is

$$D_{\mathrm{beam}}(L) = 2w(L). \tag{9}$$

Assuming perfect RIS-assisted reflection and alignment, the maximum ground coverage radius is limited by the detector FoV and link distance:

$$R_{\mathrm{cov}} = L \cdot \tan(\theta_{\mathrm{FoV}}). \tag{10}$$

This gives the radius of the coverage footprint on the horizontal x-y plane. The 2D coverage area and 3D coverage volume are expressed, respectively, as

$$A_{\mathrm{2D}} = \pi R_{\mathrm{cov}}^2, \tag{11}$$

and

$$V_{\mathrm{3D}} = \frac{1}{3}\pi R_{\mathrm{cov}}^2 h_{\mathrm{RIS}}, \tag{12}$$

where h_{RIS} is the UAV altitude. The 3D volume approximation assumes a conical beam expansion.

We assume that the RIS elements are spaced half a wavelength apart, considering i.ni.d. channels at the RIS [19]. This spacing is achieved by varying the parameters of channel fading from the composite transceiver to the RIS and from the RIS to the MRR unit. Assuming precise knowledge of the channel phase at each RIS element, the m^{th} received signal at the composite transceiver via the RIS can be expressed as [20]:

$$y_m = s_m\sqrt{P_{s_m}}H_m + n \tag{13}$$

Here, s_m is the m^{th} transmitted signal with power P_{s_m}, n is additive Gaussian noise with zero mean and variance $\sigma^2{}_n$, and H_m symbolize the channel fading resulting from the combined effects of G-G turbulence, PE, and the fog of each of the M channels of the UAV-integrated RIS-aided MRR-FSO system with diversity, which is given as:

$$H_m = h_{lm}h_{fm}h_{bm} \tag{14}$$

where h_{lm} is the fog loss for the m^{th} signal under examination and is determined through several empirical models. Specifically, the Kim model is employed due to its superior accuracy, particularly in the context of low visibility ($V \leq 6\,\mathrm{km}$) in FSO links [1]. The flat fading coefficients corresponding to the forward and backward paths of the m^{th} signal between the composite transceiver and the MRR unit in the UAV-integrated RIS-aided MRR-FSO link are provided as: $h_{f_m} = \sum_{i=1}^{N}\prod_{j=1}^{2} h_{f_{i,j,m}}$ and $h_{b_m} = \sum_{i=1}^{N}\prod_{j=1}^{2} h_{b_{i,j,m}}$. Here, $i \in \{1, 2, \ldots, N\}$ denotes the RIS element number, and

$j \in \{1, 2\}$ indicates the path (where $j = 1$ signifies the path between the CT and the i^{th} RIS element, while $j = 2$ indicates the path between the i^{th} RIS element and the MRR unit). $h_{f_{i,j,m}}$ and $h_{b_{i,j,m}}$ represent the forward and backward channel fading coefficients for the m^{th} signal and the ith RIS element within the jth path, respectively.

The primary signal degradation factors impacting the RIS-assisted connection, in addition to fog, are G-G turbulence and PE. The PDF of the G-G distribution, denoted as $f_{h_{t_m}}(h_{t_m})$, can be found in [1] as:

$$f_{h_{t_m}}(h_{t_m}) = \frac{2(\alpha_m\beta_m)^{\frac{\alpha_m+\beta_m}{2}}}{\Gamma(\alpha_m)\Gamma(\beta_m)} h_{t_m}^{\frac{\alpha_m+\beta_m}{2}-1} K_{\alpha_m-\beta_m}\left(2\sqrt{\alpha_m\beta_m h_{t_m}}\right) \tag{15}$$

Here, $h_{t_m} > 0$ denotes the channel fading coefficient due to G-G turbulence for the m^{th} signal, $\Gamma(\cdot)$ denotes the gamma function, and $K_x(\cdot)$ signifies the modified Bessel function of the second kind with order x. The parameters α_m and β_m correspond to the effective numbers of small-scale and large-scale eddies within the scattering environment, which are associated with the turbulence conditions and are defined as follows [21]::

$$\alpha_m = \left[\exp\left(\frac{0.49\sigma_{l_m}{}^2}{(1 + 0.18d_m^2 + 0.56\sigma_{l_m}{}^{12/5})^{7/6}}\right) - 1\right]^{-1} \tag{16}$$

$$\beta_m = \left[\exp\left(\frac{0.51\sigma_{l_m}{}^2(1 + 0.69\sigma_{l_m}{}^{12/5})^{-5/6}}{(1 + 0.9d_m^2 + 0.62d_m^2\sigma_{l_m}{}^{12/5})^{5/6}}\right) - 1\right]^{-1} \tag{17}$$

Here, $d_m^2 = \sqrt{k_m D^2/4L}$, where $k_m = 2\pi/\lambda_m$ denotes the optical wave number. The parameter λ_m signifies the operational wavelength associated with each of the M channels in the considered system employing WD. Furthermore, L represents the length of the optical link, and D refers to the diameter of the receiver's aperture. The term $\sigma_{l_m}{}^2$ corresponds to the Rytov variance for spherical wave propagation in a horizontal path, given by $\sigma_{l_m}{}^2 = 0.5C_n^2 k_m^{7/6} L^{11/6}$, as in [21]. Here, C_n^2 denotes the refractive index structure parameter, dependent on elevation and atmospheric conditions, and its expression is provided in [21]. The PDF of the zero-boresight PE, $f_{h_{p_m}}(h_{p_m})$, is [22]:

$$f_{h_{p_m}}(h_{p_m}) = \frac{\epsilon_m^2}{A_{o_m}^{\epsilon_m^2}} h_{p_m}^{\epsilon_m^2-1}, \quad 0 \le h_{p_m} \le A_{o_m} \tag{18}$$

where h_{p_m} signifies the channel fading coefficient due to PE for the m^{th} signal, A_{o_m} denotes the PE fading coefficient under zero PE conditions for the m^{th} signal, and ϵ_m represents the ratio between the equivalent beam radius at the destination and the PE displacement standard deviation (SD) at this destination for the m^{th} signal.

3 Closed-form statistical analysis

In this section, we present the closed-form analytical expressions for the PDF and CDF of γ by adopting an approach similar to that used in ([2], Eq. (36)), to obtain the composite channel statistics. While the intermediate derivation steps are omitted for brevity, the resulting expressions follow analogous mathematical treatment and assumptions.

We consider the generalized case where the channel coefficients $h_{f_{i,1,m}}$ and $h_{f_{i,2,m}}$ are i.ni.d, and similarly for $h_{b_{i,1,m}}$ and $h_{b_{i,2,m}}$. These coefficients are modeled as: $h_{f_{i,1,m}} = h_{t1,m}h_{p1,m}$, $h_{f_{i,2,m}} = h_{t2,m}h_{p2,m}$, $h_{b_{i,1,m}} = h_{t1,m}$, and $h_{b_{i,2,m}} = h_{t2,m}$. Here, $h_{t1,m}$ and $h_{t2,m}$ denote the G-G turbulence fading coefficients, while $h_{p1,m}$ and $h_{p2,m}$ capture the PE induced fading in the forward direction. Specifically, $h_{f_{i,1,m}}$ models the forward channel from the CT to the i^{th} RIS element for the m^{th} signal, while $h_{f_{i,2,m}}$ refers to the forward link from the i^{th} RIS element to the MRR unit. Conversely, $h_{b_{i,1,m}}$ and $h_{b_{i,2,m}}$ represent the backward paths from the CT to the RIS element and from the RIS element to the MRR unit, respectively. The composite channel fading H_m is characterized by the following PDF:

$$f_{H_m}(H_m) = \frac{\prod_{i=1}^{N}\prod_{j=1}^{2} \nu_{ri,j,m}}{H_m} \times H^{0,0:10,2;\dots;10,2}_{0,2:4,10;\dots;4,10}\left(\left\{\frac{H_m}{h_{l_m}}\prod_{j=1}^{2}\rho_{j,m}\right\}_1^N \middle| \begin{matrix} -:\left\{(1,1),(1,1),\{(\epsilon_{j,m}{}^2+1,1)\}_{j=1}^2\right\}_1^N \\ (1;\{1\}_1^N),(1;\{1\}_1^N):\left\{\{\psi_{rj,m}\}_{j=1}^2\right\}_1^N \end{matrix}\right) \tag{19}$$

where $\psi_{rj,m} = \{(\epsilon_{j,m}{}^2, 1), (\alpha_{1,j,m}, 1), (\beta_{1,j,m}, 1), (\alpha_{2,j,m}, 1), (\beta_{2,j,m}, 1)\}$, $\nu_{ri,j,m} = \nu_{fi,j,m} \quad \nu_{bi,j,m}$, and $\rho_{ri,j,m} = \rho_{fi,j,m} \quad \rho_{bi,j,m}$. $\nu_{fj,m} = \epsilon_{j,m}{}^2/\left(\Gamma(\alpha_{1,j,m})\Gamma(\beta_{1,j,m})\right)$, and $\rho_{fj,m} = (\alpha_{1,j,m}\beta_{1,j,m})/A_{o,m}$. The parameters $\alpha_{1,1,m}$ and $\beta_{1,1,m}$ represent the large-scale and small-scale characteristics of the forward path from the CT to the RIS module for the m^{th} signal, respectively. Similarly, $\alpha_{1,2,m}$ and $\beta_{1,2,m}$ describe the large-scale and small-scale aspects of the forward path from the RIS module to the MRR unit for the m^{th} signal, respectively. Moreover, $\epsilon_{1,m}$ denotes the ratio between the equivalent beam radius at the RIS module and the PE displacement SD at that module when the m^{th} signal traverses from the composite transceiver to the RIS module. Likewise, $\epsilon_{2,m}$ indicates the ratio between the equivalent beam radius at the MRR unit and the PE displacement SD at the MRR unit when the m^{th} signal travels from the RIS module to the MRR unit. In addition, $\nu_{bj,m} = 1/\Gamma(\alpha_{2,j,m})\Gamma(\beta_{2,j,m})$, and $\rho_{bj,m} = \alpha_{2,j,m}\beta_{2,j,m}$. The parameters $\alpha_{2,2,m}$ and $\beta_{2,2,m}$ represent the large-scale and small-scale parameters, respectively, of the backward path from the MRR unit to the RIS module for the m^{th} signal. Similarly, $\alpha_{2,1,m}$ and $\beta_{2,1,m}$ describe the large-scale and small-scale aspects, respectively, of the backward path from the RIS module to the composite transceiver for the m^{th} signal. For IM/DD, and after RV transformation, the PDF and

CDF of $\gamma_m = H_m^2\overline{\gamma}_m$ are derived to be as Eq. (20) and Eq. (21), respectively:

$$f_{\gamma_m}(\gamma_m) = \frac{\prod_{i=1}^{N}\prod_{j=1}^{2} \nu_{ri,j,m}}{2\gamma_m} \times H^{0,0:10,2;\ldots;10,2}_{0,2:4,10;\ldots;4,10}\left(\left\{\frac{\prod_{j=1}^{2}\rho_{rj,m}}{h_{lm}}\sqrt{\frac{\gamma_m}{\overline{\gamma}_m}}\right\}_1^N \middle|\begin{matrix} -:\left\{(1,1),(1,1),\{(\epsilon_{j,m}{}^2+1,1)\}_{j=1}^2\right\}_1^N \\ (1;\{1\}_1^N),(1;\{1\}_1^N):\left\{\{\psi_{r,j,m}\}_{j=1}^2\right\}_1^N \end{matrix}\right) \tag{20}$$

$$F_{\gamma_m}(\gamma_m) = \prod_{i=1}^{N}\prod_{j=1}^{2} \nu_{ri,j,m} \times H^{0,0:10,2;\ldots;10,2}_{0,2:4,10;\ldots;4,10}\left(\left\{\frac{\prod_{j=1}^{2}\rho_{rj,m}}{h_{lm}}\sqrt{\frac{\gamma_m}{\overline{\gamma}_m}}\right\}_1^N \middle|\begin{matrix} -:\left\{(1,1),(1,1),\{(\epsilon_{j,m}{}^2+1,1)\}_{j=1}^2\right\}_1^N \\ (1;\{1\}_1^N),(0;\{1\}_1^N):\left\{\{\psi_{r,j,m}\}_{j=1}^2\right\}_1^N \end{matrix}\right) \tag{21}$$

4 Performance analysis

4.1 Outage probability

The impact of fading on a communication system is characterized by the outage probability, which quantifies the likelihood of the SNR dropping below a specific threshold value, denoted as γ_{th}. The outage probability, represented by the equation below, is defined as the probability that the SNR, denoted by γ, is less than or equal to γ_{th}: $P_{\text{out}} = \Pr(\gamma \leq \gamma_{th}) = F_\gamma(\gamma_{th})$. Hence, using Eq. (21), we get the outage probabilities of the UAV-integrated RIS-aided MRR-FSO system with WD or TD, respectively. Assuming that the outage probability is independent for each of the M channels (acquired either through M different wavelengths or M different time slot transmissions for WD or TD schemes, respectively), the overall outage probability, denoted as P_{out} for the systems under consideration, will represent the outage probability for all M links, i.e.,:

$$P_{\text{out}} = \prod_{m=1}^{M} F_{\gamma_m}(\gamma_{th,m}) \tag{22}$$

Using Eq. (21), we conclude to the total probability of outage for the WD UAV-integrated RIS-aided MRR-FSO system:

$$P_{\text{out, WD}} = \prod_{m=1}^{M}\prod_{i=1}^{N}\prod_{j=1}^{2} \nu_{ri,j,m} \times H^{0,0:10,2;\ldots;10,2}_{0,2:4,10;\ldots;4,10}\left(\left\{\frac{\prod_{j=1}^{2}\rho_{rj,m}}{h_{lm}}\sqrt{\frac{\gamma_{th,m}}{\overline{\gamma}_m}}\right\}_1^N \middle|\begin{matrix} -:\left\{(1,1),(1,1),\{(\epsilon_{j,m}{}^2+1,1)\}_{j=1}^2\right\}_1^N \\ (1;\{1\}_1^N),(0;\{1\}_1^N):\left\{\{\psi_{r,j,m}\}_{j=1}^2\right\}_1^N \end{matrix}\right) \tag{23}$$

For evaluating the total outage probability of the considered system using TD, since we use only one pair of transceivers, therefore we are taking into account the following assumptions: $\nu_{ri,j,1} = \nu_{ri,j,2} = \cdots = \nu_{ri,j,M} = \nu_{ri,j}$, $\rho_{rj,1} = \rho_{rj,2} = \cdots = \rho_{rj,M} = \rho_{rj}$, $h_{l_1} = h_{l_2} = \cdots = h_{lM} = h_l$, $\gamma_{th,1} = \gamma_{th,2} = \cdots = \gamma_{th,M} = \gamma_{th}$, $\overline{\gamma}_1 = \overline{\gamma}_2 = \cdots = \overline{\gamma}_M = \overline{\gamma}$, $\epsilon_{j,1} = \epsilon_{j,2} = \cdots = \epsilon_{j,M} = \epsilon_j$, and $\psi_{r,j,1} = \psi_{r,j,2} = \cdots = \psi_{r,j,M} = \psi_{r,j}$, and using Eq. (23), we obtain:

$$P_{\text{out, TD}} = \left[\prod_{i=1}^{N}\prod_{j=1}^{2} \nu_{ri,j} \times H^{0,0:10,2;\ldots;10,2}_{0,2:4,10;\ldots;4,10}\left(\left\{\frac{\prod_{j=1}^{2}\rho_{rj}}{h_l}\sqrt{\frac{\gamma_{th}}{\overline{\gamma}}}\right\}_1^N \middle|\begin{matrix} -:\left\{(1,1),(1,1),\{(\epsilon_j{}^2+1,1)\}_{j=1}^2\right\}_1^N \\ (1;\{1\}_1^N),(0;\{1\}_1^N):\left\{\{\psi_{r,j}\}_{j=1}^2\right\}_1^N \end{matrix}\right)\right]^M \tag{24}$$

We should note that Eqs. (23) and (24) remain valid even in the absence of the assumption of the OC method at the receiver's end. For this metric, the sole requirement is to operate at least one of the M channels.

4.2 Average BER

The average BER serves as a metric to evaluate the reliability of data transfers. In the context of the examined UAV-integrated RIS-aided MRR-FSO systems featuring WD or TD, as well as utilizing IM/DD and OOK, its assessment is based on the assumptions outlined in Sect. 2. Specifically, these assumptions involve a single transmitter and M receivers, establishing an equivalence to a single-input multiple-output optical communication system.

In the UAV-integrated RIS-aided MRR-FSO system employing WD (TD), and taking into account OC for signal reception and following the analysis presented in [17], the average BER of the considered system with the M distinct channels can be determined as follows:

$$\overline{P}_b = \int_{\vec{\mathbf{H}}} f_{\vec{\mathbf{H}}}(\vec{\mathbf{H}}) \times Q\left(\sqrt{\frac{\sum_{i=1}^{M}\overline{\gamma}_m H_m{}^2}{2M}}\right) \tag{25}$$

where $\vec{\mathbf{H}} = [H_1, H_2, \cdots, H_m]$ represents the fading for each of the M receivers. Moreover, for the case of TD UAV-integrated RIS-aided MRR-FSO system, as mentioned earlier, the value of the average SNR is unique and thus $\overline{\gamma}_1 = \overline{\gamma}_2 = \cdots = \overline{\gamma}_M = \overline{\gamma}$. To evaluate the multiple integral of Eq. (25), we employ the approximation from [23] for the Q-function and transform it into a product of single integrals. Hence, Eq. (25) is transformed to:

$$\begin{aligned}\overline{P}_b =& \frac{1}{12}\prod_{m=1}^{M}\int_{H_m}\exp\left(-\frac{\overline{\gamma}_m H_m{}^2}{4M}\right) f_{H_m}(H_m)dH_m \\ &+ \frac{1}{4}\prod_{m=1}^{M}\int_{H_m}\exp\left(-\frac{\overline{\gamma}_m H_m{}^2}{3M}\right) f_{H_m}(H_m)dH_m\end{aligned} \tag{26}$$

Substituting Eq. (19) in Eq. (26) and expanding N-MFHF in terms of Mellin–Barnes integrals lead to:

$$\begin{aligned}\overline{P}_b =& \frac{1}{12}\prod_{m=1}^{M}\prod_{i=1}^{N}\prod_{j=1}^{2} v_{ri,j,m}\\ &\times\left(\frac{1}{2\pi\chi}\right)^N\int_0^\infty\int_{\mathcal{L}_i}\frac{H_m^{-1}}{\left(\Gamma\left(\sum_{i=1}^N \zeta_{i,m}\right)\right)^2}\\ &\times\prod_{i=1}^{N}\left\{\frac{\prod_{j=1}^2 A_{j,i,m}}{\prod_{j=1}^2\Gamma(\epsilon_{j,m}{}^2+1-\zeta_{i,m})}\left(\frac{H_m}{h_{l,m}}\prod_{j=1}^{2}\rho_{ri,j,m}\right)^{\zeta_{i,m}}\right\}\\ &\times\left\{\exp\left(-\frac{\overline{\gamma}_m H_m{}^2}{4M}\right)+3\exp\left(-\frac{\overline{\gamma}_m H_m{}^2}{3M}\right)\right\}d\zeta_{i,m}\,dH_m\end{aligned} \tag{27}$$

where $\chi=\sqrt{-1}$ is the imaginary unit, and $A_{j,i,m}=[\Gamma(\epsilon_{j,m}{}^2-\zeta_{i,m})\Gamma(\alpha_{1,j,m}-\zeta_{i,m})\Gamma(\beta_{1,j,m}-\zeta_{i,m})\Gamma(\alpha_{2,j,m}-\zeta_{i,m})\Gamma(\beta_{2,j,m}-\zeta_{i,m})[\Gamma(\zeta_{i,m})]^2]$. Expressing the exponential functions in terms of the MFHF and employing the N-MFHF definition ([24], A.1), we obtain the average BER in case of WD to be:

$$\begin{aligned}\overline{P}_{b,WD} =& \frac{1}{12}\prod_{m=1}^{M}\prod_{i=1}^{N}\prod_{j=1}^{2} v_{ri,j,m}\times\Bigg\{H^{0,1:10,2;\dots;10,2}_{2,2:4,10;\dots;4,10}\\ &\left(\left\{\frac{\prod_{j=1}^2\rho_{rj,m}}{h_{lm}}\sqrt{\frac{4M}{\overline{\gamma}_m}}\right\}_1^N\middle|\begin{matrix}(1;\{0.5\}_1^N):\left\{(1,1),(1,1),\{(\epsilon_{j,m}{}^2+1,1)\}_{j=1}^2\right\}_1^N\\(1;\{1\}_1^N),(1;\{1\}_1^N):\left\{\{\psi_{r,j,m}\}_{j=1}^2\right\}_1^N\end{matrix}\right)\\ &+3H^{0,1:10,2;\dots;10,2}_{2,2:4,10;\dots;4,10}\\ &\left(\left\{\frac{\prod_{j=1}^2\rho_{rj,m}}{h_{lm}}\sqrt{\frac{3M}{\overline{\gamma}_m}}\right\}_1^N\middle|\begin{matrix}(1;\{0.5\}_1^N):\left\{(1,1),(1,1),\{(\epsilon_{j,m}{}^2+1,1)\}_{j=1}^2\right\}_1^N\\(1;\{1\}_1^N),(1;\{1\}_1^N):\left\{\{\psi_{r,j,m}\}_{j=1}^2\right\}_1^N\end{matrix}\right)\Bigg\}\end{aligned} \tag{28}$$

Utilizing Eq. (28) and considering the aforementioned assumptions for the TD UAV-integrated RIS-aided MRR-FSO scheme, the expression for estimating the average BER of this FSO link with TD is presented as:

$$\begin{aligned}\overline{P}_{b,TD} =& \frac{1}{12}\left[\prod_{i=1}^{N}\prod_{j=1}^{2} v_{ri,j,m}\right]^M\\ &\times\Bigg\{\Bigg[H^{0,1:10,2;\dots;10,2}_{2,2:4,10;\dots;4,10}\\ &\left(\left\{\frac{\prod_{j=1}^2\rho_{rj}}{h_l}\sqrt{\frac{4M}{\overline{\gamma}}}\right\}_1^N\middle|\begin{matrix}(1;\{0.5\}_1^N):\left\{(1,1),(1,1),\{(\epsilon_j{}^2+1,1)\}_{j=1}^2\right\}_1^N\\(1;\{1\}_1^N),(1;\{1\}_1^N):\left\{\{\psi_{r,j}\}_{j=1}^2\right\}_1^N\end{matrix}\right)\Bigg]^M\\ &+3\Bigg[H^{0,1:10,2;\dots;10,2}_{2,2:4,10;\dots;4,10}\\ &\left(\left\{\frac{\prod_{j=1}^2\rho_{rj}}{h_l}\sqrt{\frac{3M}{\overline{\gamma}}}\right\}_1^N\middle|\begin{matrix}(1;\{0.5\}_1^N):\left\{(1,1),(1,1),\{(\epsilon_j{}^2+1,1)\}_{j=1}^2\right\}_1^N\\(1;\{1\}_1^N),(1;\{1\}_1^N):\left\{\{\psi_{r,j}\}_{j=1}^2\right\}_1^N\end{matrix}\right)\Bigg]^M\Bigg\}\end{aligned} \tag{29}$$

4.3 Maximum effective bit rate

In TD, the same information signal is transmitted multiple times over different time slots to enhance reliability by treating each transmission as an independent event. The receiver combines these independent receptions to improve overall communication reliability, effectively mitigating the impact of fading or other transmission impairments. However, as the number of time slots M increases, there exists a trade-off between reliability and data transmission rate. A larger M value results in more redundant transmissions, increasing the duration for sending the complete message. While this redundancy improves the chances of successful reception, it comes at the cost of reducing the maximum rate of data transmission. Hence, the maximum effective bit rate (R_{eff}) is less than the maximum bit rate of the link. This trade-off between reliability and efficiency is crucial in designing UAV-integrated RIS-aided MRR-FSO systems, emphasizing the need to carefully balance reliability requirements with desired data transfer speeds based on the specific application and system constraints.

The maximum achievable bit rate in a channel characterized by fast fading statistics is determined by its average capacity. Importantly, this approach involves a singular point-to-point link with one transmitter and one receiver, where the average channel capacity serves as the ultimate metric for the maximum bit rate. Considering that the TD scheme involves the transmission of the same information bits M times, the effective bit rate is given by:

$$\begin{aligned}R_{eff} =&\frac{1}{M}\mathbb{E}[\log_2(1+\frac{e}{2\pi}\gamma_m)]\\ =&\frac{1}{M}\int_0^\infty\log_2\left(1+\frac{e}{2\pi}\gamma_m\right)f_{\gamma_m}(\gamma_m)d\gamma_m\end{aligned} \tag{30}$$

Substituting Eq.(20) in (30), use the definition of N-MFHF, and reverse the integration order to obtain:

$$\begin{aligned}R_{eff} =&\frac{\prod_{i=1}^N\prod_{j=1}^2 v_{ri,j}}{2M\ln(2)h_l}\left(\frac{1}{2\pi\chi}\right)^N\int_0^\infty\gamma^{-1}\ln\left(1+\frac{e}{2\pi}\gamma\right)\\ &\times\prod_{i=1}^{N}\int_{\mathcal{L}_i}\frac{A_i(\zeta_i)\left(\rho_{ri,j}\times\sqrt{\frac{\gamma}{\overline{\gamma}}}^{\zeta_i}\right)^{\zeta_i}}{\left(\prod_{j=1}^2\Gamma(\epsilon_j{}^2+1-\zeta_i)\right)\left(\Gamma(\sum_{i=1}^N\zeta_i)\right)^2}d\zeta_i d\gamma\end{aligned} \tag{31}$$

where $A_i(\zeta_i)=\prod_{j=1}^2[\Gamma(\epsilon_j{}^2-\zeta_i)\Gamma(\alpha_{1,j}-\zeta_i)\Gamma(\beta_{1,j}-\zeta_i)\Gamma(\alpha_{2,j}-\zeta_i)\Gamma(\beta_{2,j}-\zeta_i)[\Gamma(\zeta_i)]^2]$. Solving the inner integral solution in (29), we obtain

$$\begin{aligned}&\int_0^\infty\gamma^{-1+\frac{1}{2}\sum_{i=1}^N\zeta_i}\ln\left(1+\frac{e}{2\pi}\gamma\right)d\gamma\\ &=\frac{1}{2\pi j}\times\int_{\mathcal{L}}\frac{\Gamma(-u+1)(\Gamma(u))^2}{\Gamma(u+1)}\times\left(\frac{e}{2\pi}\gamma\right)^u du\end{aligned} \tag{32}$$

Applying the final-value theorem and using the definition of N-MFHF in ([24], A.1), we get:

$$\mathrm{R}_{\mathrm{eff}} = \frac{\prod_{i=1}^{N}\prod_{j=1}^{2}\nu_{ri,j}}{2M\ln(2)} \times H^{0,1:10,2;\ldots;10,2;1,1}_{1,2:4,10;\ldots;4,10;1,1}\left(\left\{\frac{\prod_{j=1}^{2}\rho_{rj}}{h_{lRIS}\sqrt{\delta\overline{\gamma}}}\right\}_{1}^{N}, \frac{e}{2\pi\delta}\left|\begin{matrix}(1;\{0.5\}_1^N,1):(1,1),\left\{(1,1),(1,1),\{(\epsilon_j{}^2+1,1)\}_{j=1}^{2}\right\}_1^N \\ \Psi_x,\Psi_x:\left\{\{\psi_{rj}\}_{j=1}^{2}\right\}_1^N,(0,1)\end{matrix}\right.\right) \tag{33}$$

where δ is in the order 10^{-6}.

5 Results and discussion

In this section, we present numerical evaluations to assess the performance of UAV-integrated RIS-aided MRR-FSO links utilizing the IM/DD detection technique. The analysis is grounded in realistic system configurations and parameters, making it applicable to actual deployments in the field.

The RIS panel is modeled as a dielectric-based metasurface fabricated from low-loss materials, such as silicon or titanium dioxide (TiO_2), on a glass substrate [25]. These materials are commonly used in optical RIS implementations due to their favorable transmission and reflection characteristics. Each RIS element has a size of $\lambda/2$, approximately 775 nm at the operating wavelength of 1550 nm, which is standard for FSO communication. Simulated array sizes include $N = 5$, 10, and 15 elements, representing small-to-moderate arrays compatible with UAV payload constraints. The reflectivity and phase control of each RIS element are modeled with a programmable resolution of 2–3 bits, consistent with commercially available modules in the visible and near-infrared domains [25].

The MRR terminal consists of a corner-cube retroreflector combined with a modulator, which may utilize technologies such as MEMS, liquid crystals, or quantum wells. These modulators are capable of supporting data rates from several Mbps up to tens of Mbps, consistent with the practical constraints and capabilities of UAV platforms powered by batteries. Passive retroreflection and low-power modulation are prioritized to enhance energy efficiency, based on experimental demonstrations in prior studies.

At the receiver, an avalanche photodiode (APD) is employed, operating at a central wavelength of 1550 nm. The APD is characterized by a sensitivity of −35 dBm and an aperture diameter of 1 cm. The field of view (FoV) is set to $\theta_{\mathrm{FoV}} = 2°$, and the beam divergence is defined as $\theta_d = 1.5$ mrad [26].

The modulation speed was assumed to range from a few megabits per second (Mbps) up to tens of Mbps, based on performance metrics reported in existing MEMS- and liquid crystal-based MRR implementations. To enable UAV integration, power consumption considerations were critical; therefore, the system design emphasized passive retroreflection and low-power modulation, supported by findings from existing experimental studies demonstrating feasibility for battery-powered platforms.

The geometry of the optical channel includes a total link distance of 1000 m, divided into two 500 m segments: one from the CT to the RIS and the other from the RIS to the MRR. The altitudes are configured as follows: $h_{\mathrm{CT}} = 50$ m, $h_{\mathrm{RIS}} = 100$ m, and $h_{\mathrm{MRR}} = 50$ m. The optical RIS is positioned midway between the CT and the MRR terminal to maximize reflective gain and beam alignment efficiency.

Environmental degradation is modeled through fog attenuation, atmospheric turbulence, and PEs. Fog attenuation is computed using the Kim model [27]. Atmospheric turbulence is modeled using the G-G distribution. The refractive index structure parameter C_n^2 is set to 6×10^{-14} and $20 \times 10^{-14}\,\mathrm{m}^{-2/3}$ for moderate and strong turbulence, respectively. The fading parameters α_m and β_m are derived based on established models for turbulence in optical systems [21]. PEs are incorporated using $\epsilon_{1,m} = 1.3$ and $\epsilon_{2,m} = 1.1$, with the zero-pointing-error amplitude set to $A_{0,m} = 1$ [2].

To evaluate system performance, we apply the MFHF implementation in MATLAB, as demonstrated in previous work [2], to assess the analytical expressions provided in earlier studies. These expressions are used to calculate two key performance metrics: outage probability and average BER, for both WD and TD schemes. The validity of the analytical results is verified by MC simulations with over 4×10^6 independent trials.

WD is evaluated using typical FSO wavelengths: 850 nm, 980 nm, 1064 nm, 1310 nm, and 1550 nm. These wavelengths align with atmospheric transmission windows to minimize attenuation and are widely supported by commercial photonic components. For each of the $M = 1, 2, 3$ signal copies used in WD, an individual photodetector is assumed to be tuned to a distinct λ_m.

While TD schemes typically reduce the bit rate due to signal repetition, we estimate the maximum achievable bit rate under TD evaluated as a function of the number of signal copies M and other system parameters. The numerical results presented in this section illustrate the outage probability and average BER under various settings, offering insight into the influence of parameters such as RIS array size N, number of channels M, wavelength λ_m, and turbulence level C_n^2 on system efficiency.

All parameters are consistent with current technological capabilities and are inspired by prior experimental works. Where possible, datasheet-level parameter ranges are matched to existing commercial modules such as those from Thorlabs. While this work is focused on analytical modeling and performance evaluation, the chosen parameter sets are based on physically realizable components. These updates ensure that the study is not only theoretically grounded but also experimentally relevant and repeatable with available or near-future hardware.

In the following subsections, we analyze the 2D and 3D coverage, comparing the proposed system with the baseline UAV-FSO system (Sect. 5.1), followed by an investigation of techniques for combining the transmission link output signals at the destination to generate a signal resilient to fading. The studied diversity techniques include the WD technique (Sect. 5.2) and the TD technique (Sect. 5.3).

5.1 2D and 3D coverage: proposed system vs. baseline UAV-FSO

MATLAB simulations are conducted to evaluate the spatial SNR performance over a range of user locations in both 2D and 3D space. A user location is considered "covered" if the composite channel SNR satisfies the condition SNR $\geq \gamma_{th} = 5$ dB. As illustrated in Fig. 2, the results indicate that the proposed RIS-MRR system provides a substantial improvement in spatial coverage over the baseline UAV-FSO system. This improvement can be attributed to several crucial factors, each playing a role in the system's enhanced performance.

A key factor behind this improvement is the enhanced beam steering and directional control provided by the RIS. The RIS offers dynamic adjustment of the signal's propagation direction, allowing for precise beam alignment. This adaptability helps the system respond to changes in user positions and environmental factors, thereby optimizing signal strength and expanding coverage areas. In contrast with the baseline UAV-FSO system, which generally relies on fixed beam orientations, the RIS can continuously modify the beam to ensure optimal signal quality across a wider area.

Furthermore, the capability to establish indirect connections via the MRR greatly improves the system's robustness. In situations where direct LoS links are blocked by physical obstacles or interference, the RIS-MRR system can generate alternative indirect links. This ability to form indirect connections ensures reliable communication in challenging conditions, thereby broadening the coverage area and strengthening network resilience when compared to the baseline UAV-FSO system.

The RIS also contributes to a better overall SNR distribution. By carefully adjusting the transmitted optical signal, it helps to boost the signal quality at the user's location, particularly in areas where the baseline UAV-FSO system might suffer from reduced SNR due to factors such as longer distances, atmospheric attenuation, or beam misalignment. This capability to improve SNR ensures that the system remains efficient, even under less ideal conditions.

Additionally, the RIS's capacity to adapt to changing environmental factors, like atmospheric turbulence, helps to reduce path loss. By modifying its reflection properties, the RIS can counteract the effects of path loss over extended distances, ensuring that the transmitted signal maintains stronger power levels over a larger area. This adaptability is especially valuable in sustaining stable communication quality across different distances and environmental conditions.

An additional benefit of the RIS-MRR system is the spatial diversity it offers. The RIS can modify the direction of signal propagation to bypass obstacles or regions

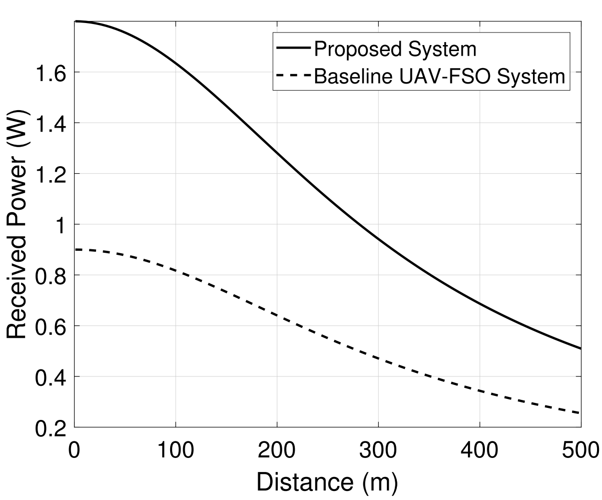

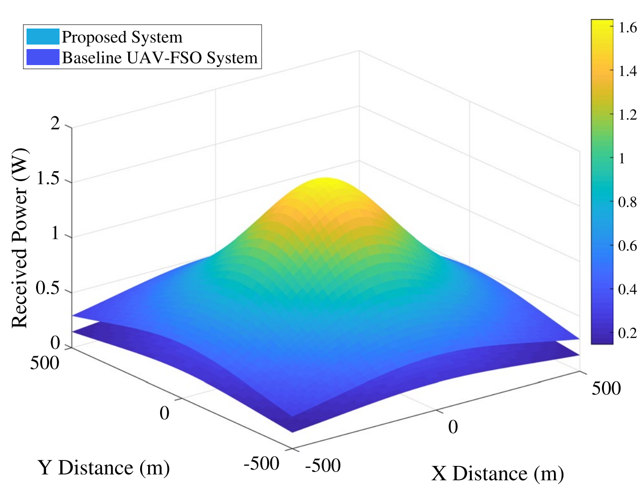

Fig. 2 Comparison of spatial coverage for the proposed UAV-integrated RIS-aided MRR-FSO system and the baseline UAV-FSO system: **a** 2D coverage and **b** 3D coverage

where signal quality may deteriorate. This spatial diversity guarantees that more areas receive adequate SNR, even in non-line-of-sight (NLoS) conditions. By redirecting signals along the most favorable paths, the system ensures coverage in regions where conventional systems might struggle.

The RIS-MRR system also provides built-in scalability and flexibility, which makes it well-suited for dynamic environments. As user density and mobility rise, the RIS-MRR system can adjust to various user locations and network setups. On the other hand, the baseline UAV-FSO system is typically constrained by fixed beam directions, which limits its ability to adapt to such dynamic changes.

Finally, the integration of RIS and MRR components boosts the system's ability to withstand environmental disturbances like turbulence and atmospheric scattering. These factors usually reduce the performance and coverage of conventional UAV-FSO systems. However, the adaptive features of the RIS-MRR system enable it to sustain stable communication in fluctuating atmospheric conditions, ensuring dependable performance even in difficult environments.

In conclusion, the proposed RIS-MRR system offers a distinct advantage over the baseline UAV-FSO system, thanks to its versatile beam steering, ability to form indirect links, enhanced SNR distribution, reduced path loss, spatial diversity, scalability, and resilience to environmental disturbances. These features collectively contribute to an extended spatial coverage and enhanced performance across a wide range of user locations and environmental conditions.

5.2 Wavelength diversity

For the WD case, we consider the same five wavelengths previously mentioned. Additionally, we assume that the average electrical SNR and sensitivity limits are uniform across all M receivers, i.e., $\overline{\gamma}_1 = \overline{\gamma}_2 = \cdots = \overline{\gamma}_M = \overline{\gamma}$, and $\gamma_{th,1} = \gamma_{th,2} = \cdots = \gamma_{th,M} = \gamma_{th}$. The threshold SNR is $\gamma_{th} = 5$ dB. First, we use Eqs. (23) and (28) to evaluate the outage probability, $P_{\text{out, WD}}$, versus the normalized average electrical SNR, $\overline{\gamma}/\gamma_{th}$, and the average BER, $\overline{P}_{b,WD}$, as a function of the average electrical SNR, $\overline{\gamma}$, for three diversity configurations: no diversity, and diversity orders $M = 2$ and $M = 3$, considering the aforementioned values of C_n^2. The obtained results are shown in Figs. 3 and 4 for three scenarios, namely with $N = \{5, 10, 15\}$.

As illustrated in Fig. 3, the outage probability of a UAV-integrated RIS-assisted MRR-FSO system employing WD exhibits a pronounced reduction with an increasing number, M, of distinct wavelength channels. This behavior remains consistent for a fixed value of C_n^2 and a constant N. For instance, at $N = 5$ and under moderate atmospheric turbulence, without diversity (i.e., $M = 1$), the system achieves an outage probability of 10^{-1} at 20 dB. In contrast, for $M = 2$, it reaches 2×10^{-2}, and for $M = 3$, it attains 10^{-3} at the same normalized average SNR. Conversely, for $N = 5$ and strong atmospheric turbulence, the outage probabilities are 0.13, 0.04, and 9×10^{-3} for the cases of no diversity, $M = 2$, and $M = 3$, respectively, at 20 dB. This trend remains consistent for $N = 10$ and $N = 15$.

Similarly, as shown in Fig. 4, the average BER of the considered system employing WD also experiences a marked decrease with increasing M. For example, at $N = 5$ and under moderate atmospheric turbulence, the system achieves an average BER of 9.6×10^{-2} without diversity. In comparison, it drops to 9×10^{-3} for $M = 2$, and further to 6×10^{-4} for $M = 3$ at 20 dB. Under strong atmospheric turbulence and the same N, the average BERs are 9.8×10^{-2}, 0.5×10^{-2}, and 6×10^{-3} for the cases of no diversity, $M = 2$, and $M = 3$, respectively. Similar behavior is observed for $N = 10$ and $N = 15$.

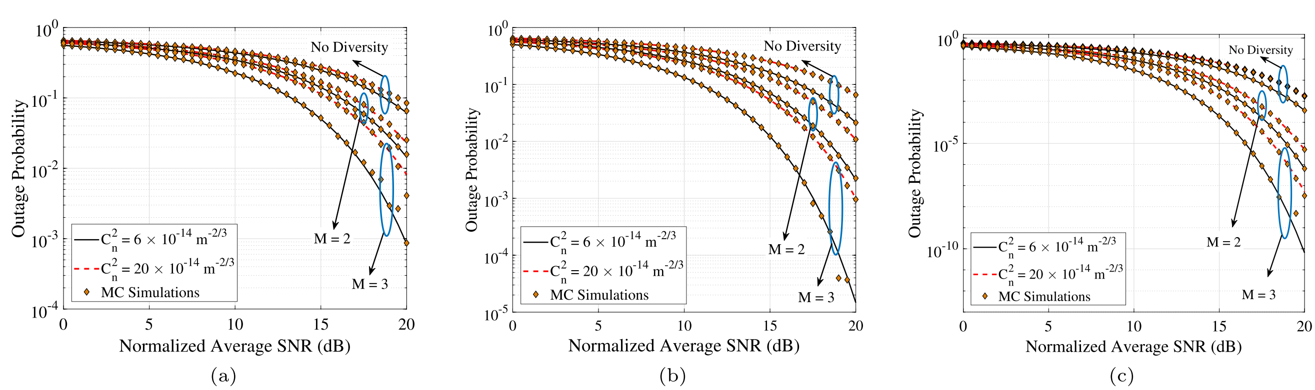

Fig. 3 Outage probability for a UAV-integrated RIS-assisted MRR-FSO system with WD, versus the normalized average electrical SNR in dB: **a** when $N = 5$, **b** when $N = 10$, and **c** when $N = 15$

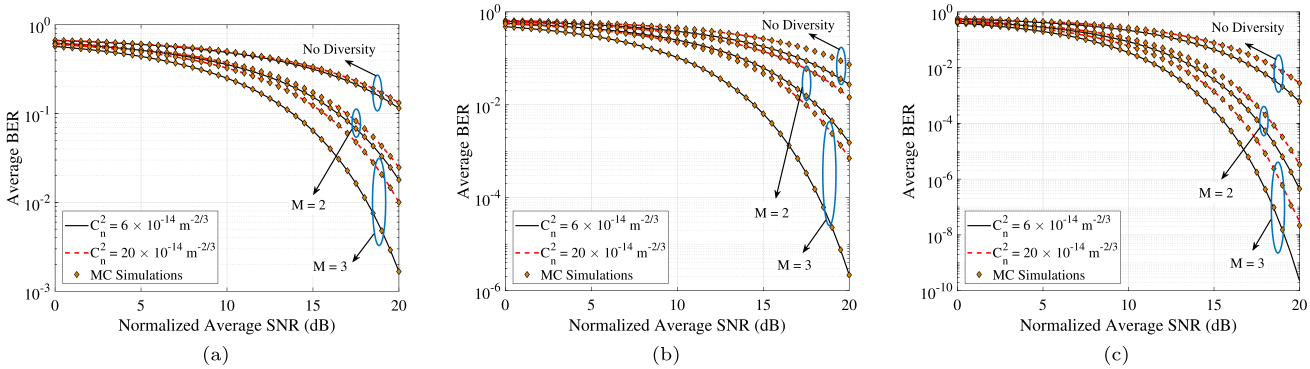

Fig. 4 Average BER for a UAV-integrated RIS-assisted MRR-FSO system with WD, versus the average electrical SNR in dB: **a** when $N = 5$, **b** when $N = 10$, and **c** when $N = 15$

The observed performance improvements are attributed to the increased diversity gain, which provides additional independent communication channels that help mitigate fading. In FSO communications, diversity through wavelength channels facilitates interference averaging under turbulent atmospheric conditions. Using multiple, well-separated wavelength channels ensures uncorrelated fading events, thereby reducing the probability of simultaneous deep fades and improving both outage probability and average BER.

Employing multiple wavelength channels also helps overcome atmospheric losses and absorption variations, ensuring that at least some channels remain relatively unaffected, contributing to overall system resilience.

As expected, for a fixed M and given N, weaker atmospheric turbulence (i.e., smaller C_n^2) results in lower outage probability and average BER. This is due to reduced fluctuations in the air's refractive index, which diminishes scintillation effects and stabilizes the received optical signal.

Finally, increasing the number of RIS elements, N, enhances system performance. For example, with $M = 3$ and under moderate atmospheric turbulence, the outage probability is 10^{-3}, 2×10^{-5}, and 9×10^{-11} for $N = 5$, 10, and 15, respectively, while the average BER is 6×10^{-4}, 2×10^{-7}, and 10^{-12} for the same respective values. The increased number of RIS elements enables more advanced beamforming and signal steering capabilities. Combined with WD, this significantly mitigates fading caused by atmospheric turbulence, enhancing the system's adaptability, interference mitigation, and overall reliability.

The close agreement between the analytical and MC simulation results confirms the correctness of the derived equations and demonstrates that our theoretical framework accurately models the system's performance under realistic channel conditions.

5.3 Time diversity

For the case of TD-FSO systems, we fix the operational wavelength at $\lambda = 1550$ nm. Additionally, like WD, we assume that the average electrical SNR and sensitivity limits are uniform across all M receivers. The threshold SNR is $\gamma_{th} = 5$ dB. First, we use Eqs. (24) and (29) to estimate the outage probability, $P_{\text{out, TD}}$, versus the normalized average electrical SNR, $\overline{\gamma}/\gamma_{th}$, and the average BER, $\overline{P}_{b,TD}$, as a function of the average electrical SNR, $\overline{\gamma}$, for no diversity, $M = 3$, and $M = 5$, considering the aforementioned values of C_n^2. The obtained results are shown in Figs. 5 and 6 for three scenarios, namely with $N = \{5, 10, 15\}$.

As illustrated in Fig. 5, the outage probability of a UAV-integrated RIS-assisted MRR-FSO system employing TD experiences a pronounced reduction with an increasing number, M, of distinct time slots. This behavior holds steady for a fixed value of C_n^2 and a constant N. For instance, at $N = 5$ and under moderate atmospheric turbulence, with no diversity, the system achieves an outage probability of 3×10^{-2} at 20 dB. In contrast, for $M = 3$, it reaches 6×10^{-4}, and for $M = 5$, it attains 1.5×10^{-5} at the same normalized average SNR. Conversely, for $N = 5$ and strong atmospheric turbulence, the outage probabilities are 8×10^{-2}, 2×10^{-3}, and 2×10^{-4} for no diversity, $M = 3$, and $M = 5$, respectively, at 20 dB. This behavior holds consistent for $N = 10$ and $N = 15$.

In a similar manner, as illustrated in Fig. 6, the average BER of the considered system employing TD experiences a pronounced reduction with an increasing number, M, of distinct time slots. This behavior holds steady for a fixed value of C_n^2 and a constant N. For instance, at $N = 5$ and under moderate atmospheric turbulence, with no diversity, the system achieves an average BER of 2×10^{-2} at 20 dB. In contrast, for $M = 3$, it reaches 1.5×10^{-4}, and for $M = 5$, it attains 10^{-5} at the same average SNR. Conversely, for $N = 5$ and strong atmospheric turbulence, the average BERs are

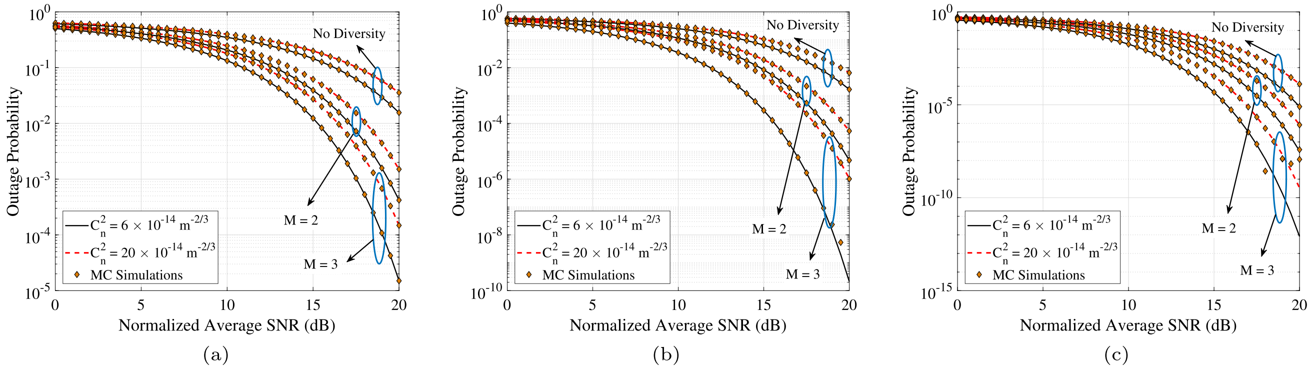

Fig. 5 Outage probability for a UAV-integrated RIS-assisted MRR-FSO system with TD, versus the normalized average electrical SNR in dB: **a** when $N = 5$, **b** when $N = 10$, and **c** when $N = 15$

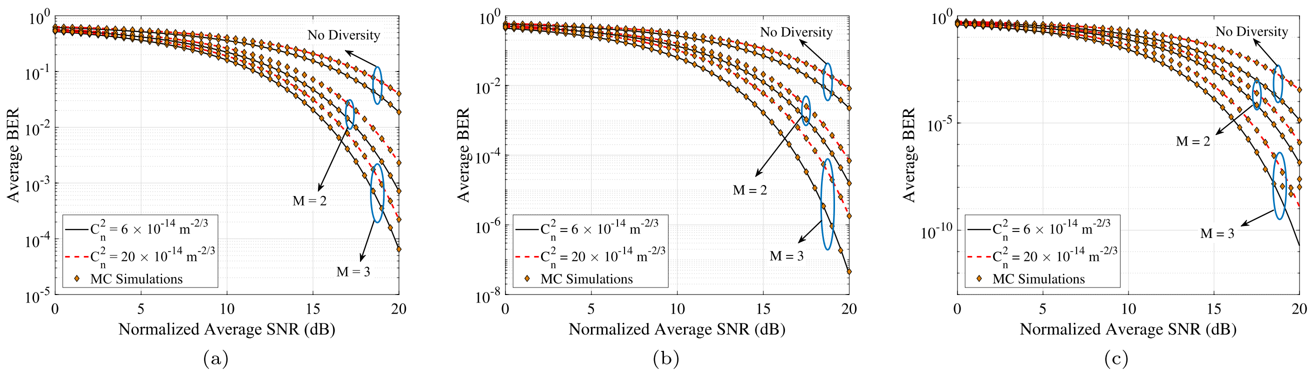

Fig. 6 Average BER for a UAV-integrated RIS-assisted MRR-FSO system with TD, versus the average electrical SNR in dB: **a** when $N = 5$, **b** when $N = 10$, and **c** when $N = 15$

3×10^{-2}, 9.5×10^{-4}, and 5×10^{-5} for no diversity, $M = 3$, and $M = 5$, respectively, at 20 dB. This behavior holds consistent for $N = 10$ and $N = 15$.

Hence, increasing the number of time slots for TD in a FSO communication system contributes to a reduction in outage probability and average BER. This improvement can largely be attributed to the advantages of diversity techniques in reducing the negative impacts of atmospheric turbulence and other channel impairments. Atmospheric turbulence induces random variations in the air's refractive index, resulting in scintillation and fading of the optical signal. By using TD, where signals are transmitted in different time slots, the effects of turbulence are averaged out, lowering the chances of experiencing deep fades simultaneously across all time slots. Furthermore, TD helps reduce interference from various atmospheric conditions, thus boosting the overall reliability of the system. It also creates opportunities for error correction methods, such as Forward Error Correction, which enhance the system's ability to withstand errors. Overall, the use of TD in FSO systems provides redundancy and averaging, making the system more robust and resulting in a lower outage probability and average BER. Importantly, this better performance is achievable in the case of TD without the need for additional transceivers, while in the WD case, additional transceivers are necessary.

As expected, like the case of WD, for constant M and a certain value for N, weaker atmospheric turbulence (i.e., lower C_n^2) corresponds to a lower outage probability and lower average BER.

Finally, as with WD, increasing the number N of RIS elements enhances system performance. For example, with $M = 5$ and under moderate atmospheric turbulence, the outage probability is 1.5×10^{-5}, 0.5×10^{-10}, and 10^{-12} for $N = 5$, 10, and 15, respectively, and the average BER is 10^{-5}, 9×10^{-10}, and 8×10^{-14} for $N = 5$, 10, and 15, respectively.

Conversely, higher values of M lead to a reduction in the maximum effective bit rate transmission, as defined by Eq. (33), whereas, for the WD technique, it remains constant. This reduction can be attributed to several factors. Firstly, there is an increase in overhead due to the management and coordination of transmissions across these slots, encompassing synchronization, signaling, and coordination mechanisms. This heightened overhead consumes a significant portion of available time, leaving less time for actual data transmission. Additionally, the increase in the number of time slots leads to reduced duration available for transmitting data in each slot, resulting in lower effective bit rates for each time slot and impacting the overall system's maximum effective bit rate. Furthermore, atmospheric conditions introduce variations in channel characteristics over time, and with a large M, the channel may exhibit more variability between time slots, posing challenges in maintaining consistent link quality and potentially causing increased errors and re-transmissions. The effectiveness of TD, relying on differences in channel conditions over time to combat fading, may diminish with a large M due to smaller differences between consecutive time slots, reducing diversity gain. Finally, the benefits of TD in combating fading may saturate as the number of time slots increases, particularly in scenarios with severe fading, limiting the potential for proportional increases in diversity gain and improvement in the effective bit rate under challenging conditions. Hence, Fig. 7 illustrates the maximum effective bit rate for three values of N, three values of M, and two values of the refractive index structure parameter. It is evident that employing this technique allows for a decrease in both the outage probability and the average BER. However, this improvement comes at the cost of a simultaneous mandatory reduction in the maximum effective bit rate transmission. All figures show that the MC simulations agree highly with the evaluation of the analytical expressions.

The close agreement between the analytical and MC simulation results confirms the correctness of the derived equations and demonstrates that our theoretical framework accurately models the system's performance under realistic channel conditions.

Both WD and TD improve system reliability by reducing outage probability and average BER, especially under strong turbulence. Increasing diversity order M enhances performance, but comes with trade-offs-WD needs more complex, wavelength-specific hardware, while TD sacrifices throughput with additional time slots. A larger number of RIS elements N improve beamforming, making the system more robust in harsh conditions like urban or disaster zones. Combining RIS with diversity techniques ensures stable operation in challenging environments, including coastal or mountainous areas.

WD offers low latency and high throughput, ideal for real-time applications like UAV telemetry, but requires multiple transceivers, suiting resource-rich platforms. TD, using a single transceiver, is more power-efficient and better for lightweight UAVs or portable systems. However, increasing M in TD reduces effective bit rate, so designers must balance reliability and speed. For optimization, choose low-absorption wavelengths (e.g., 1310 nm, 1550 nm) in WD, and adjust M in TD based on application needs. In all cases, increasing RIS elements improves system performance when budget and payload allow.

The proposed UAV-integrated RIS-aided MRR-WD/TD-FSO system offers a streamlined architecture that significantly improves performance while reducing hardware and energy requirements compared to existing UAV-FSO solutions. By leveraging passive MRRs at user terminals, the system eliminates the need for optical receivers, minimizing both size and power usage—ideal for UAVs with limited payload and energy capacity. The inclusion of RIS modules enables adaptive beam steering without the computational load of active relays, and WD/TD schemes introduce manageable complexity while substantially enhancing reliability. This makes the system suitable for energy-constrained UAVs, portable ground units, and real-time applications such as UAV emergency response in urban and NLoS conditions.

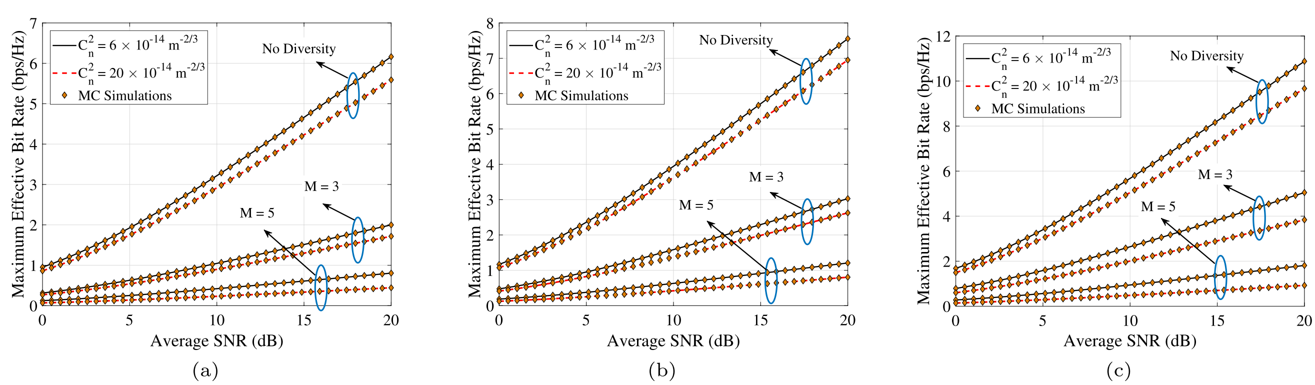

Fig. 7 Maximum effective bit rate for a UAV-integrated RIS-assisted MRR-FSO system with TD, versus the average electrical SNR in dB: **a** when $N = 5$, **b** when $N = 10$, and **c** when $N = 15$

Notably, the system achieves an average BER of 1.2×10^{-6} at 20 dB SNR-surpassing conventional UAV-FSO (9.5×10^{-4}), RIS-only (3.8×10^{-5}), and hybrid relay-based (2.1×10^{-5}) systems [5, 28, 29] . It also reduces outage probability below 0.02, compared to around 0.25 for traditional setups [17]. WD enhances spectral efficiency via parallel multi-wavelength transmission, while TD offers a cost-effective option for lightweight platforms. The use of passive RIS and MRR components lowers CAPEX and enables rapid, reconfigurable deployments in remote or mobile scenarios. With its balance of performance, simplicity, and energy efficiency, this system is a strong candidate for future 6 G networks and UAV-assisted FSO links in dynamic or disaster-prone environments.

6 Conclusions and future work

This paper presented a comprehensive evaluation of UAV-integrated RIS-assisted MRR-FSO systems, emphasizing the performance gains achievable through the integration of WD and TD techniques. WD enhances link reliability under adverse atmospheric conditions by enabling multi-wavelength transmission, while TD mitigates signal fading and multipath effects. Despite their benefits, WD introduces implementation complexity and potential channel interference, whereas TD may reduce maximum bit rates—necessitating careful trade-off analysis.

Future work will expand the theoretical model to incorporate realistic factors such as UAV mobility, atmospheric variations, and combined scattering and absorption. We also aim to examine temporal fading correlations and UAV-induced Doppler shifts through stochastic trajectory modeling. Additionally, we will conduct asymptotic performance analysis in high-SNR and high-diversity regimes, deriving closed-form expressions for outage probability and BER. These insights will guide system design and validate the effectiveness of WD and TD under practical deployment constraints.

Author contributions Amr AbdElKader wrote the main manuscript text, and all authors reviewed the manuscript.

Data availability No datasets were generated or analyzed during the current study.

Declarations

Conflict of interest The authors have no relevant financial or non-financial interests to disclose.

Ethical approval Not applicable.

References

1. Mohamed, P.H., El-Shimy, M.A., Shalaby, H.M.H., Kheirallah, H.N.: FSO channel modelling and performance evaluation over dust combined with GG atmospheric turbulence. In: 2023 40th National Radio Science Conference (NRSC), vol. 1, pp. 121–130. IEEE, (2023)
2. AbdElKader, A.G., Allam, A., Kato, K., Shalaby, H.M.H.: Performance enhancement of RIS-assisted MRR-UOWC systems using the spectral-power-efficient LQAM-MPPM. Opt. Commun., pp. 130444 (2024)
3. Zhong, X., Chen, C., Wen, W., Liu, M., Fu, H.Y., Haas, H.: Optimization of surface configuration in IRS-aided MIMO-VLC: a ber minimization approach. IEEE Photon. J. (2024)
4. Chapala, V.K., Zafaruddin, S.M.: Intelligent connectivity through RIS-assisted wireless communication: exact performance analysis with phase errors and mobility. IEEE Trans. Intell. Veh. (2023)
5. Singh, D., Swaminathan, R.: Comprehensive performance analysis of hovering UAV-based FSO communication system. IEEE Photonics J. **14**(5), 1–13 (2022)
6. Lin, Q., Guanjun, X., Zeng, Z., Zhang, N., Zhang, Q.: UAV-assisted RF/FSO relay system for space-air-ground integrated network: a performance analysis. IEEE Trans. Wireless Commun. **21**(8), 6211–6225 (2022)
7. Li, D., Xu, G., Gao, M., Song, Z., Zhang, Q., Zhang, W.: Performance analyses of RIS-assisted stochastic UAV mmWave relay communication system with moment matching estimation. IEEE Wirel. Commun. Lett. (2024)
8. Yang, G., Zhang, J., Zhang, J., Bi, M., Chen, T., You, S., Zhou, X., Wang, T., Li, J., Geng, H.: Wavefront compensation with the micro corner-cube reflector array in modulating retroreflector free-space optical channels. J. Lightw. Technol. **39**(5), 1355–1363 (2020)
9. Dabiri, M.T., Rezaee, M., Mohammadi, L., Javaherian, F., Yazdanian, V., Hasna, M.O., Uysal, M.: Modulating retroreflector based free space optical link for UAV-to-ground communications. IEEE Trans. Wireless Commun. **21**(10), 8631–8645 (2022)
10. Kim, S.-J., Han, S.-K.: Estimation and performance analysis of multiple incident beam misalignment in spatial diversity based FSO transmissions. Opt. Commun. **521**, 128618 (2022)
11. Huang, Q., Wen, W., Liu, M., Pengfei, D., Chen, C.: Energy-efficient unmanned aerial vehicle-aided visible light communication with an angle diversity transmitter for joint emergency illumination and communication. Sensors **23**(18), 7886 (2023)
12. Balaji, K.A., Prabu, K.: Performance evaluation of FSO system using wavelength and time diversity over Malaga turbulence channel with pointing errors. Opt. Commun. **410**, 643–651 (2018)
13. Li, Y.: Ultra-reliable and low-latency communications for unmanned aerial vehicles networks (2024)
14. Kirubakaran, N.: Enhanced mobile broadband in 5 era: addressing demand for high-speed connectivity for the future of mobile data services (2024)
15. Ntabeni, U., Basutli, B., Alves, H., Chuma, J.: Device-level energy efficient strategies in machine type communications: power, processing, sensing, and RF perspectives. IEEE Open J. Commun. Soc. (2024)
16. Varotsos, G.K., Nistazakis, H.E., Aidinis, K., Jaber, F., Rahman, K.K.M.: Transdermal optical wireless links with multiple receivers in the presence of skin-induced attenuation and pointing errors. Computation **7**(3), 33 (2019)
17. Wang, Y., Zhu, L., Feng, W.: Performance study of wavelength diversity serial relay OFDM FSO system over exponentiated Weibull channels. Opt. Commun. **478**, 126470 (2021)
18. Ding, Z., Chen, J., He, C. and Jin, R.: Elevation and azimuth direction finding by two-element pattern reconfigurable antenna array.

IEEE Trans. Antennas Propagation **70**(3), 2261–2270 (2021). IEEE
19. Hongyang, D., Zhang, J., Cheng, J., Ai, B.: Millimeter wave communications with reconfigurable intelligent surfaces: performance analysis and optimization. IEEE Trans. Commun. **69**(4), 2752–2768 (2021)
20. Selimis, D., Peppas, K.P., Alexandropoulos, G.C., Lazarakis, F.I.: On the performance analysis of RIS-empowered communications over Nakagami-m fading. IEEE Commun. Lett. **25**(7), 2191–2195 (2021)
21. Luan, X., Yue, P., Yi, X.: Scintillation index of an optical wave propagating through moderate-to-strong oceanic turbulence. JOSA A **36**(12), 2048–2059 (2019)
22. AbdElKader, A.G., Allam, A., Kato, K., Shalaby, H.M.H.: Performance enhancement of MRR underwater optical communications using LQAM-MPPM. In: 2022 Asia Communications and Photonics Conference (ACP), pp. 473–476. IEEE (2022)
23. Soranzo, A., Vatta, F., Comisso, M., Buttazzoni, G., Babich, F.: Explicitly invertible approximations of the Gaussian Q-function: a survey. IEEE Open J. Commun. Soc. **4**, 3051–3101 (2023)
24. Mathai, A.M., Saxena, R.K., Haubold, H.J.: The H-function: Theory and Applications. Springer, Berlin (2009)
25. Ullah, N., Zhao, R., Huang, L.: Recent advancement in optical metasurface: fundament to application. Micromachines **13**(7), 1025 (2022)
26. Kaymak, Y., Rojas-Cessa, R., Feng, J., Ansari, N., Zhou, M.: On divergence-angle efficiency of a laser beam in free-space optical communications for high-speed trains. IEEE Trans. Veh. Technol. **66**(9), 7677–7687 (2017)
27. Mohamed, P.H., El-Shimy, M.A., Shalaby, H.M.H., Kheirallah, H.N.: Hybrid FSO/RF system over proposed random dust attenuation model based on real-time data combined with G–G atmospheric turbulence. Optics Communications **549**, 129891 (2023)
28. Ndjiongue, A.R., Ngatched, T.M.N., Dobre, O.A., Armada, A.G., Haas, H.: Analysis of RIS-based Terrestrial-FSO link over GG turbulence with distance and jitter ratios. J. Lightw. Technol. **39**(21), 6746–6758 (2021)
29. Salhab, A.M., Yang, L.: Mixed RF/FSO relay networks: RIS-equipped RF source vs RIS-aided RF source. IEEE Wirel. Commun. Lett. **10**(8), 1712–1716 (2021)

Amr G. AbdElKader received his B.Sc. degree in Electrical Engineering and M.Sc. degree in Engineering Physics from Alexandria University, Alexandria, Egypt, in 2010 and 2019, respectively. He earned his Ph.D. from the Egypt-Japan University of Science and Technology (E-JUST), Alexandria, Egypt, in 2025. From March 2011 to January 2019, he worked as a demonstrator, and from January 2019 to January 2025, he served as a teaching assistant. He is currently an Assistant Professor in the Department of Engineering Physics at Alexandria University. His research interests include the design of photonic communication systems.

Ahmed Allam received the B.Sc. degree in electrical engineering from Alexandria University, Alexandria, Egypt, and the M.Eng. and Ph.D. degrees from the University of Alberta, Edmonton, AB, Canada. From April 1994 to January 1998, he worked as an Instrument Engineer with Schlumberger. From May 2000 to September 2001, he was with Murandi Communications Ltd., Calgary, AB, Canada, where he worked on RF transceivers' design. From April 2007 to April 2008, he worked on RF CMOS transceivers' design with Scanimetrics Inc., Edmonton, AB. He is currently a Professor with the Department of Electronics and Communications Engineering, Egypt-Japan University of Science and Technology, Alexandria. His research interests include the design of RF circuits and systems.

Kazutoshi Kato received the B.S and M.S. degrees in physics and the Ph.D. degree from Waseda University in 1985, 1987, and 1993, respectively. Since 1987, he has been with NTT Opto-Electronics Laboratories, where he had been engaged in research on receiver OEIC's, high-speed p-i-n PD's for wideband transmissions. From 1994 to 1995, he was on leave from NTT at France Telecom CNET Bagneux Laboratory, France, as a Visiting Researcher working on high-sped PD's. From 2000 to 2003, he was with NTT Electronics Corporation, where he was involved in developing photonic network systems. From 2004 to 2011, he was a Research Manager at the NTT Photonics Laboratories, where he is in charge of developing semiconductor devices and subsystems for photonic network systems. From 2012 he has been a professor at Kyushu University. His current research topics are terahertz-wave technologies for a wireless transmission, and tunable lightwave technologies for a photonics network.

Hossam M. H. Shalaby received the B.S. and M.S. degrees in electrical engineering from Alexandria University, Alexandria, Egypt, in 1983 and 1986, respectively. He earned the Ph.D. degree in electrical engineering from the University of Maryland at College Park, USA, in 1991. He joined the Electrical Engineering Department at Alexandria University in 1991 and was promoted to Professor in 2001. He is currently on leave from Alexandria University. Since August 2024, he has been a Professor with the Department of

Electrical Engineering and Computer Science, College of Engineering, University of Toledo, USA. From August 2023 to August 2024, he was with the Department of Electrical and Computer Engineering, University of Memphis, Tennessee, USA. From September 2010 to August 2016, he served as the Chair of the Department of Electronics and Communications Engineering at the Egypt-Japan University of Science and Technology (E-JUST), Alexandria, Egypt. He also held academic appointments at the International Islamic University Malaysia (September 1996--January 1998) and at the School of Electrical and Electronic Engineering, Nanyang Technological University, Singapore (February 1998-- February 2001). His research interests include quantum communications and information, as well as photonics systems and networks. He is a Senior Member of both the IEEE Photonics Society and Optica (formerly the Optical Society of America, OSA).